



# Fe/P dual-doping NiMoO<sub>4</sub> with hollow structure for efficient hydrazine oxidation-assisted hydrogen generation in alkaline seawater

Zhan Zhao<sup>a</sup>, Zizhen Li<sup>a,\*</sup>, Zisheng Zhang<sup>b</sup>, Xiangchao Meng<sup>a,\*</sup>

<sup>a</sup> Key Laboratory of Marine Chemistry Theory and Technology (Ministry of Education), College of Chemistry & Chemical Engineering, Ocean University of China, Qingdao, Shandong 266100, China

<sup>b</sup> Department of Chemical and Biological Engineering, Faculty of Engineering, University of Ottawa, Ottawa, Ontario K1N6N5, Canada

## ARTICLE INFO

### Keywords:

Seawater splitting  
Hollow structure  
Hydrogen evolution reaction  
Hydrazine oxidation reaction  
Dual-doping

## ABSTRACT

Electrosynthesis of hydrogen straightforwardly from seawater represents a potential solution towards carbon-neutral economy. However, with the sluggish oxygen evolution reaction (OER) at anode, the sustainable and cost-effective application is greatly hindered by extra energy consumption and serious chlorine chemistry in seawater. Herein, based on the advanced hydrazine-assisted electrolysis strategy, we reported a trifunctional Fe, P dual-doping NiMoO<sub>4</sub> nanorods with a hollow structure for highly active hydrogen evolution reaction (HER) (23 mV @ 10 mA cm<sup>-2</sup>) and OER (213 mV @ 10 mA cm<sup>-2</sup>) activity, which also significantly decreased the cell voltage (activity variation for ~1.40 V) in two-electrode system by replacing OER with thermodynamically beneficial hydrazine oxidation reaction (HzOR). Notably, a record low electricity expense of 2.3 kW h m<sup>-3</sup> was obtained among commercial reactor in alkaline seawater/0.5 M N<sub>2</sub>H<sub>4</sub>. Meanwhile, the corrosion resistance of catalyst allows stable catalytic performance in seawater without any ClO<sup>-</sup> generation. Density functional theory calculations showed that Fe/P co-doping effectively endowed optimized electronic structure and modulated d-band centre for intermediates adsorption/desorption.

## 1. Introduction

Limited fossil fuel supplies and serious pollution to environment are calling for nature-friendly emission economy, in which the green hydrogen (H<sub>2</sub>) plays an important role as sustainable energy carrier [1–6]. Electrocatalytic hydrogen evolution reaction straightforwardly from water is attractive for promoting green development in terms of carbon neutrality and economic availability [7–9]. However, it should be noted that large quantities of purity-water as feedstock has been considered as a bottleneck especially in the area that lacks freshwater resources [10–13]. Fortunately, the seawater guarantees more sustainable and flexible solution for large-scale hydrogen production via water electrolysis, which accounts for ~97% of the global water reserve [14,15]. Moreover, the seawater electrolysis provides a potential strategy to coastal areas, which could produce high-purity water from seawater in the process of producing energy. On the other hand, coupling seawater electrolysis with offshore wind power could effectively reduce the cost of electricity transmission and solve the issue of volatile renewable energy. Despite the potential benefit, one of the critical barriers for seawater splitting is competitive chlorine electro-oxidation reactions

(ClOR) at anode, which not only leads to severe anode corrosion thus resulting in reduced electrolysis efficiency but also causes environmental hazards by toxic and corrosive chlorine species (ClO<sup>-</sup>) [16–19]. Although the hypochlorite formation can be suppressed in alkaline seawater by oxygen evolution reaction (OER) kinetic overpotential below 480 mV [20], the availability of large-scale industrial hydrogen production (>500–1000 mA cm<sup>-2</sup>) may be significantly minimized [21]. Meanwhile, another formidable challenge of seawater splitting is the thermodynamically unfavorable water oxidation (1.23 V vs. RHE), wherein the sluggish multiple proton/electron-transfer and complex adsorption/desorption of intermediates caused high energy consumption during direct seawater splitting [22]. Guided by such general trend, replacing the tardy OER with electro-oxidation of hydrazine oxidation reaction (HzOR; N<sub>2</sub>H<sub>4</sub> + 4OH<sup>-</sup> → N<sub>2</sub> + 4H<sub>2</sub>O + 4e<sup>-</sup>) provides a promising strategy for yielding hydrogen with high electrolysis efficiency [23]. The low theoretical potential value (−0.33 V vs. RHE) holds significant potential in regard to electricity consumption for hydrogen production, which also provides the extra-benefit in refraining from chlorine chemistry with high potential gap (2.05 V) [24]. On the other hand, hydrazine sewage as toxic material may be harmful to the human

\* Corresponding authors.

E-mail addresses: [lizizhen@ouc.edu.cn](mailto:lizizhen@ouc.edu.cn) (Z. Li), [mengxiangchao@ouc.edu.cn](mailto:mengxiangchao@ouc.edu.cn) (X. Meng).

<https://doi.org/10.1016/j.apcatb.2024.123805>

Received 15 November 2023; Received in revised form 6 January 2024; Accepted 31 January 2024

Available online 3 February 2024

0926-3373/© 2024 Elsevier B.V. All rights reserved.

health and ecosystem, which is free source from deoxidant in industry [25]. Therefore, coupling the electrolysis of costless seawater and degradation of hydrazine in industrial sewage as anodic half-reaction is expected to be a two-in-one strategy for cost-effective hydrogen production and ecosystem protection, as shown in Fig. 1. However, it is still challenging to explore high-activity multifunctional electrocatalysts for overall hydrazine splitting.

Among recently reported non-noble catalysts, transition metal molybdate compounds, such as  $\text{NiMoO}_4$  and  $\text{CoMoO}_4$ , have been investigated as promising and scalable candidates owing to superior chemical stability and abundant reserves [26,27]. Especially, the combination of molybdenum oxides and 3d transition metal play a vital role in turning the water dissociation and  $\text{H}_2$  adsorption ability [7]. Unfortunately, there is still much room for transition metal molybdate compound in term of high-performance, which is subject to poor electrical conductivity, sparse active sites and low specific area. Hetero atom doping (Fe, Co, Ni, Ru, P, W *et.al*), as an effective tactic to tailor electronic properties around active sites, has been devoted to fabricate high active electrocatalysts with more electrochemical active sites regarding the HzOR-assisted  $\text{H}_2$  production [17]. Among metal cation, the octahedral  $\text{Fe}^{3+}$  site in molybdate compounds was characterized small Fe-O bond length, which obtained intense adsorption ability with multiple O-containing intermediates and led to multi-fold improvement of the activity for OER [28]. Meanwhile, it has been reported that the introduction of Fe could enhance active site - O covalency and thus resulting to oxyl character and higher OER activity [29]. On the other hand, many theoretical and experimental researches in terms of anions doping have been reported, which was beneficial to the stability of seawater splitting [30,31]. Typically, the P anion not only played an important role of strengthening chemical bonding but also activated the active planes with increased interlayer spacing, which tended to generate P - O species as passivation layer [30]. For example, Zhang *et al.* realized low cell voltage ( $28 \text{ mV @ } 10 \text{ mA cm}^{-2}$ ) for two-electrode configuration containing P, W dual-doped  $\text{Co}_3\text{N}$  nanowire array electrode in  $1.0 \text{ M KOH}$  with  $0.1 \text{ M N}_2\text{H}_4$  electrolyte [32]. Despite enormous achievements of heteroatom doping for enhanced intrinsic properties, the most of transition metal molybdate compounds was characterized with solid counterparts, wherein the low surface area and loading capacity were uncondusive to further improve the electrocatalytic performance. Benefited by extra void spaces, microstructural strategies has attracted great research interest, which endows catalysts desirable electrochemically active sites, rapid electron diffusion and even efficient mass diffusion among electrode-electrolyte-gas three-phase interface [33]. It can be concluded that the effect of heteroatom doping and structural merits will greatly enhance the electrochemical activity of transition metal molybdate compounds, but is still tough to assemble these mentioned advantages into an electrocatalyst. Meanwhile, it is also highly desired to in-depth understand the electronic redistribution by theoretical calculation.

Inspired by the above strategies, we reported an integrated

electrocatalyst composed of Fe, P dual-doping  $\text{NiMoO}_4$  nanorods with a hollow structure (donated as Fe/P- $\text{NiMoO}_4$ ), which worked as highly active trifunctional electrode for HER/OER and HzOR in alkaline seawater. Particularly, the hollow structure endowed catalysts with rich electrochemically active sites and enhanced mass diffusion kinetic. Benefitting from the coupling effect of Fe, P co-doping as well as unique hollow structure, the as-synthesized Fe/P- $\text{NiMoO}_4$  exhibited superior HER ( $23 \text{ mV @ } 10 \text{ mA cm}^{-2}$ ) and OER ( $213 \text{ mV @ } 10 \text{ mA cm}^{-2}$ ) activity compared with state-of-the-art electrocatalysts. Excitingly, the introduction of Fe/P- $\text{NiMoO}_4$  among hybrid seawater electrolysis realized energy-saving seawater splitting without hypochlorite production in alkaline seawater/ $0.5 \text{ M N}_2\text{H}_4$  electrolyte. Moreover, commercial membrane electrode assembly (MEA) stack using Fe/P- $\text{NiMoO}_4$  in alkaline seawater/ $0.5 \text{ M N}_2\text{H}_4$  required ultralow operation energy consumption of  $2.3 \text{ kW h m}^{-3}$  for overall hydrazine splitting (OHS), indicating the remarkable advantage among overall seawater splitting (OWS) and hydrazine splitting. Meanwhile, the corrosion resistance of catalyst allowed stable catalytic performance in seawater without any  $\text{ClO}^-$  generation. Finally, in-depth DFT calculation revealed that the Fe/P doping could not only led to metallic property with enhanced electrical conductivity but also modulate *d*-band centre causing enhanced adsorption between molecule and intermediates. This work offered a strategy for rational design of highly efficient doped catalysts with morphological engineering for cost-effective hydrogen generation and hydrazine degradation-based seawater splitting.

## 2. Experimental section

### 2.1. Fabrication of $\text{NiMoO}_4$

First, commercial Ni foam (donated as NF, thickness: 1 mm) was cut into  $3 \times 4 \text{ cm}^2$ , and successively cleaned with HCl solution for 30 min and deionized water for 10 min under ultrasonication to remove the oxide layer on the surface. Then, the pretreated NF and  $(\text{NH}_4)_2\text{Mo}_2\text{O}_7 \cdot 4 \text{ H}_2\text{O}$  ( $0.01 \text{ M}$ ) were added into aqueous solution ( $75 \text{ mL}$ ) of  $\text{Ni}(\text{NO}_3)_2 \cdot 6 \text{ H}_2\text{O}$  ( $0.04 \text{ M}$ ). After continuously stirring for 30 min, the reaction was conducted in sealed Teflon-lined stainless autoclave at  $150^\circ \text{C}$  for 6 h in an oven. Finally, the obtained  $\text{NiMoO}_4$  was taken out and washed with deionized water and ethanol to neutral before being fully dried at  $80^\circ \text{C}$ . All the synthesized catalysts were loaded on the NF, wherein the naming of catalysts was omitted NF.

### 2.2. Synthesis of PBA@ $\text{NiMoO}_4$

Typically, one piece of  $\text{NiMoO}_4$  precursor and  $\text{K}_3[\text{Fe}(\text{CN})_6]$  ( $4 \text{ mg mL}^{-1}$ ) aqueous solution was transferred into  $100 \text{ mL}$  Teflon liner, which was conducted at  $85^\circ \text{C}$  for 2 h. After cooling down naturally to room temperature, the product was taken out and washed by deionized water and ethanol several times to neutral, which was donated as PBA@ $\text{NiMoO}_4$  and the PBA represent Prussian blue analogues.

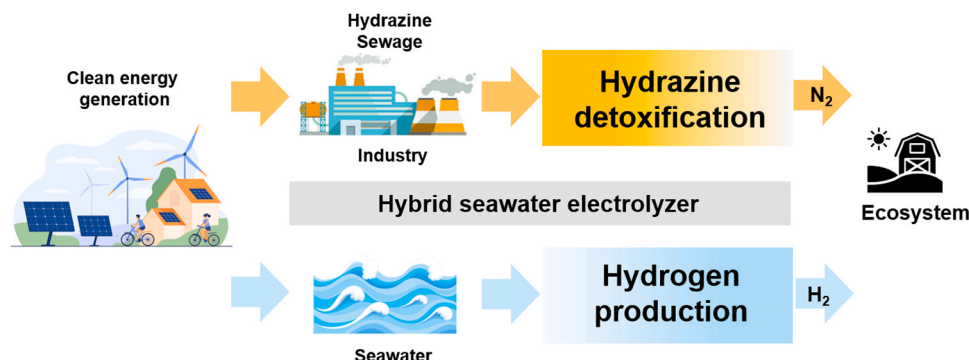


Fig. 1. Schematic illustration of eco-friendly hydrogen production with renewable electricity, low-cost seawater and industrial hydrazine sewage.

### 2.3. Synthesis of Fe/P-NiMoO<sub>4</sub>

In a typical phosphating procedure, one piece of PBA@NiMoO<sub>4</sub> precursor and 1.5 g NaH<sub>2</sub>PO<sub>4</sub>·H<sub>2</sub>O were placed in porcelain boat, which was annealed at 400 °C for 2 h with a heating rate of 5 °C min<sup>-1</sup> under 200 sccm N<sub>2</sub> flow (cooling rate of 10 °C min<sup>-1</sup>). Then, Fe/P-NiMoO<sub>4</sub> were obtained after the system cooled down naturally. For comparison, P-NiMoO<sub>4</sub> was synthesized as fabrication procedure of Fe/P-NiMoO<sub>4</sub> by replacing the PBA@NiMoO<sub>4</sub> with NiMoO<sub>4</sub> in the annealing reaction. Similarly, the P-PBA was synthesized by replacing the PBA precursor of PBA@NiMoO<sub>4</sub>. Typically, for the preparation of PBA precursor, the cleaned NF was immersed into aqueous solution (10 mL) of FeCl<sub>3</sub>·6 H<sub>2</sub>O (0.05 M) and K<sub>3</sub>[Fe(CN)<sub>6</sub>] (0.1 M). After continuously stirring for 1 min, the product was taken out and washed by deionized water and ethanol several times to neutral before being fully dried at 80 °C.

### 2.4. Characterization

The X-ray diffraction (XRD, Rigaku Miniflex 600) was conducted to obtain the crystal structure and chemical composition, which ranged from 5 to 90° with Cu Kα radiation (λ = 1.5405 Å). Meanwhile, the valence states of elements on surface was characterized by X-ray photoelectron spectroscopy (XPS, Thermo Scientific K-Alpha). The structural morphologies and energy-dispersive spectroscopy (EDS) analysis were characterized by the scanning electron microscopy (SEM, Zeiss Gemini 300) and transmission electron microscopy (TEM, JEOL JEM 2100). The Brunauer-Emmett-Teller (BET) surface area and porous structures of catalysts were conducted by Micromeritics ASAP 2460. The Zeta potential values of NiMoO<sub>4</sub>, PBA@NiMoO<sub>4</sub> and Fe/P-NiMoO<sub>4</sub> were obtained by Malvern Zetasizer Nano ZS to analyze the electrification.

### 2.5. Electrochemical measurements

Electrochemical tests were applied with three-electrode system by CHI660E to evaluate the electrochemical performance of the samples, wherein the saturated calomel electrode was utilized as reference electrode, the platinum sheet electrode worked as counter electrode and as-synthesized electrocatalysts grown on NF were directly employed as working electrode, respectively. For the preparation of commercial Pt/C and RuO<sub>2</sub> electrodes, 10 mg catalysts powder was dispersed into 1 mL solution (Nafion: ethanol = 1: 9) under ultrasonic condition, which was dropped on the surface of pretreated NF.

For the half-cell HER/OER test, the electrolyte was alkaline seawater (pH 14) and the real seawater was collected in the South Yellow Sea (35°55'E, 120°42'N). In detail, the elements of Ca<sup>2+</sup> and Mg<sup>2+</sup> in seawater were observed in the form of white precipitate and alkaline seawater was obtained by filtration. The linear sweep voltammetry test (LSV) were collected with 95% iR compensation at 5 mV s<sup>-1</sup> for the catalytic performance of these catalysts, which could be transferred to the Tafel slope. The measured potentials were calibrated to the reversible hydrogen electrode (RHE) as following Nernst equation: (E<sub>RHE</sub> = E<sub>SCE</sub> + 0.098 V + 0.0592 × pH). Electrochemical impedance spectroscopy (EIS) was carried out from 0.01 Hz to 1000 kHz with 5 mV amplitude. Chronopotentiometric tests of the Fe/P-NiMoO<sub>4</sub> were performed at different current density to evaluate long-term stability. To measure the double-layer capacitance values (C<sub>dl</sub>), the cyclic voltammetry (CV) curves were conducted in the non-Faradaic current area with different scanning rate. For the half-cell HzOR test, all the measurements were performed as the same conditions of HER/OER, excepting the electrolyte was replaced by alkaline seawater with 0.5 M N<sub>2</sub>H<sub>4</sub>.

The two-electrode configuration was assembled for the overall seawater splitting and overall hydrazine splitting. The test in membrane electrode assembly (MEA, YJ-MEA-2020) was conducted by using anion-exchange membrane (FAA-3-50) between homemade electrode, wherein the electrolyte was cycled by the peristaltic pump. The LSV curves were recorded without iR compensation at 5 mV s<sup>-1</sup> and the

stability test of the two-electrode configuration was recorded at the controlled potential. The Faradaic efficiencies of system was calculated by the amount of gaseous products measuring with the water drainage method among chronopotentiometry in different seawater electrolyte, which could be obtained as following equation:  $\frac{N_M}{N_T}$ ;  $N_T = Q \times 22.4/nF$ , where the  $N_M$  was the gaseous products,  $Q$  was the transferred electrons in system,  $F$  was the Faraday constant ( $n = 2$  for HzOR,  $n = 2$  for HER,  $n = 4$  for OER),  $N_T$  was the theoretical gaseous products. The H<sub>2</sub> turn-over frequency (TOF) was examined by the CV test among PBS solution (PH = 7) from -0.2 V to 0.6 V vs. RHE, which was calculated by the following equation:  $\text{TOF} = I/(F \times n \times M)$ , where  $I$  was the current density from LSV curves,  $n$  was the transferred electrons in system ( $n$  was 2 for HER,  $n = 4$  for OER),  $M$  was the measured active sites in electrode.

### 2.6. Measurement of hydrazine

The content of hydrazine in electrolyte could be measured by the Watt and Chrisp method, wherein the colour reagent solution was prepared by mixing the (dimethylamino) benzaldehyde (5.99 g), ethanol (300 mL) and HCl (30 mL). For the determination of Hydrazine degradation, quantitative anolyte was collected per 20 min and diluted with 5 mL HCl (1 M), which was mixed with 5 mL colour reagent solution under sufficiently stirring and measured by UV-vis spectrum at λ = 457 nm.

### 2.7. Measurement of hypochlorite

The content of hypochlorite in electrolyte could be measured by the colourimetric method, wherein the color reagent solution was prepared by mixing the N, N-diethyl-1,4-phenylenediamine sulfate (1.1 g/L) and phosphate buffer (pH = 6.5). For the determination of hypochlorite degradation, quantitative anolyte was collected per 12 h and diluted with HCl (1 M), which was mixed with colour reagent solution under sufficiently stirring and measured by UV-vis spectrum at λ = 550 nm.

### 2.8. Density functional theory (DFT) calculation

All DFT calculations were conducted by the Vienna ab initio Simulation Package (VASP)[34], wherein the exchange functional was depicted by the Perdew-Burke-Ernzerhof (PBE) functional and generalized gradient approximation (GGA)[35,36]. In our structure, the projector augmented wave (PAW) method was applied to classify the ion cores with a plane-wave cutoff energy of 300 eV, and 3 × 3 × 1 k-point mesh was set. Meanwhile, for geometry optimization, the energy convergence criterion was performed to -0.01 eV and 10<sup>-5</sup> eV/Å. Moreover, to avoid the correlation between two adjacent structure, a 20 Å vacuum space was set in the z direction.

## 3. Results and discussion

### 3.1. Synthesis and structural characterization of Fe/P-NiMoO<sub>4</sub>

A hollow structural and self-supported Fe/P-NiMoO<sub>4</sub> electrode was successfully designed aiming to propel hybrid seawater splitting by facilitating the ability to release gases and improve the intrinsic electrochemical activity. The preparation route was shown in Fig. 2a. Typically, the commercial NF was chosen as conductive support due to the superior conductivity and high surface area (Fig. S1). First, the precursors were added in the DI water with desired ratio and then the pretreated NF was immersed in that, which was incubated in sealed Teflon-lined stainless autoclave under certain condition to form solid NiMoO<sub>4</sub> nanorod (detailed condition in experimental section). Then, the NiMoO<sub>4</sub> precursor was transferred to PBA@NiMoO<sub>4</sub> catalyst with the hollow nanorod structures via a self-sacrificing template process[37]. Finally, the Fe/P-NiMoO<sub>4</sub> catalyst was consequently fabricated through



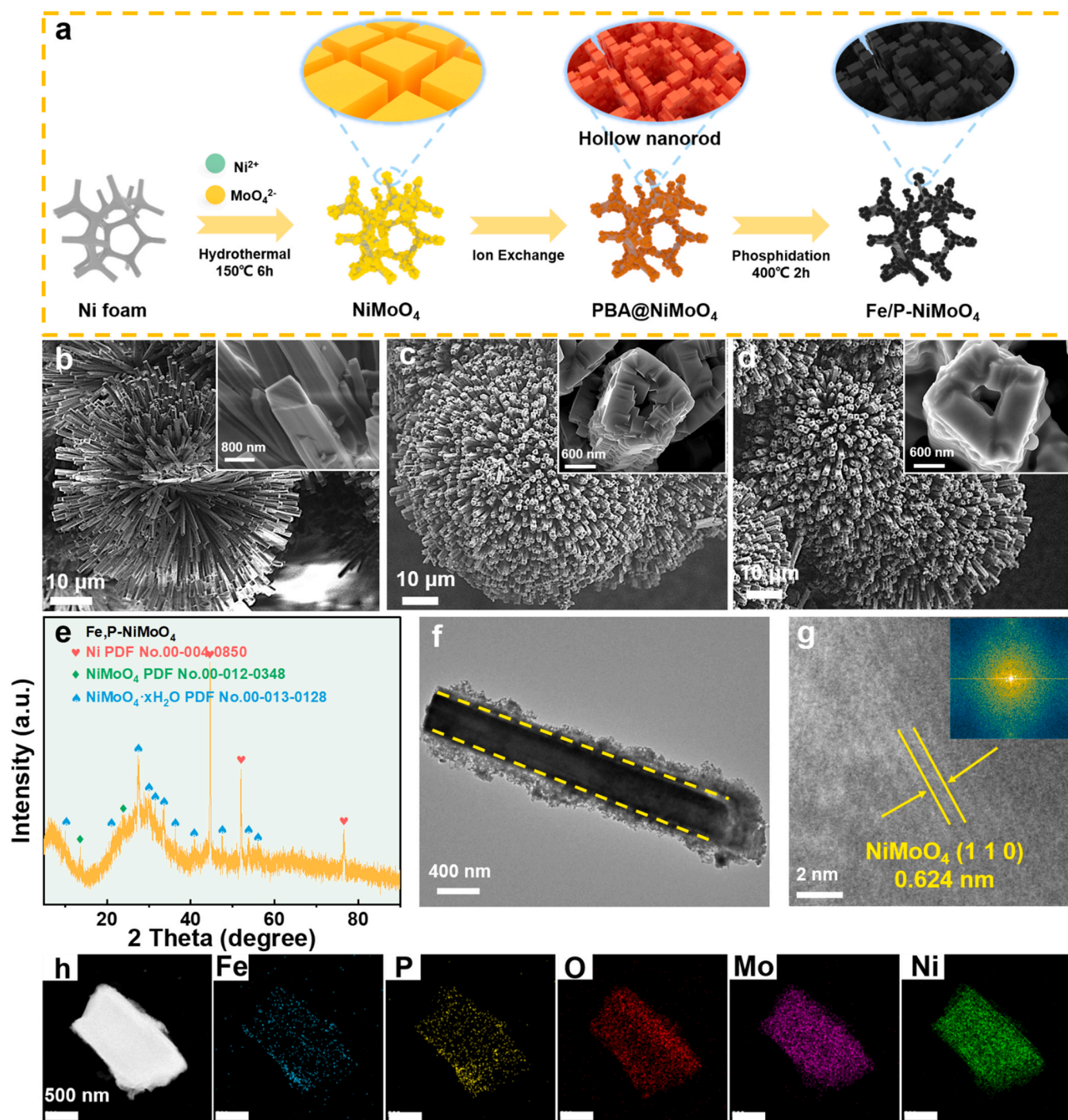


**Fig. 2.** (a) Schematic illustration of the fabrication process of Fe/P-NiMoO<sub>4</sub>. SEM images of (b) NiMoO<sub>4</sub>, (c) PBA@NiMoO<sub>4</sub> and (d) Fe/P-NiMoO<sub>4</sub>. (e) XRD pattern of Fe/P-NiMoO<sub>4</sub>. (f, g) TEM image of Fe/P-NiMoO<sub>4</sub>. (h) the HAADF image and EDS images of Fe/P-NiMoO<sub>4</sub>.

phosphorization reaction. The SEM images of as-prepared samples exhibited the typical morphology at different stages. First, as shown in Fig. 2b and S2, nanorods-shaped NiMoO<sub>4</sub> were densely and uniformly aligned on the NF matrix, which constituted hierarchical microsphere with an average diameter of 30 ~ 50  $\mu\text{m}$ . After the NiMoO<sub>4</sub> precursor was immersed in K<sub>3</sub>[Fe(CN)<sub>6</sub>] aqueous solution, the nanorod-like structure was still maintained. It should be noted that the PBA nanocubes with the size of 300 ~ 500 nm stacked together to form strange hollow nanorods (Fig. 2c). As was revealed from Fig. 2d, the prepared Fe/P-NiMoO<sub>4</sub> still exhibited well-distributed hollow structure with smooth surface after subsequent thermal phosphating procedure.

Moreover, the Fe/P-NiMoO<sub>4</sub> was investigated by XRD patterns to evaluate the crystal structure as displayed in Fig. 2e, wherein the clear diffraction peaks at 10.0°, 13.5°, 20.9°, 23.8°, 27.6°, 29.8°, 31.7°, 33.4°, 36.3°, 41.1°, 47.5°, 53.9°, 55.8° could be well pointed to NiMoO<sub>4</sub> phase (PDF No.00-012-0348 and PDF No.00-013-0128). By comparing the XRD patterns of NiMoO<sub>4</sub> (Fig. S3), there was no appearance of new species, which unveiled that presence of Fe and P dopants did not affect the dominant phase of NiMoO<sub>4</sub>. The XRD results of PBA@NiMoO<sub>4</sub> and P-NiMoO<sub>4</sub> were also shown in Fig. S4. Meanwhile, structure analyses examined by TEM (Fig. 2f) indicated similar structure with PBA@NiMoO<sub>4</sub> and further showed interplanar distance of 0.624 nm (Fig. 2g),



which were well ascribed to the (1 1 0) crystal plane of  $\text{NiMoO}_4$ , consistent with XRD result. The above observations improved that co-dopants maintained primary phase and morphology of  $\text{NiMoO}_4$ . In addition, the EDS mapping analysis was implemented (Fig. 2h) to demonstrated the coexistence and uniform distribution of Mo, Ni, O, Fe, and P indicating successful doping of Fe and P elements. The detailed atomic ratio of P: O: Ni: Fe: Mo  $\approx$  1.16: 13.58: 53.70: 1.23: 30.33, was shown in EDS spectrum (Fig. S5). The relatively low content of P and Fe elements further indicated the formation of heterogeneous atom among  $\text{NiMoO}_4$ .

Typically, the hollow nanorod array structure of  $\text{PBA@NiMoO}_4$  could be synthesized by the in-situ ion exchange process (Fig. 3a). At first, the  $\text{Ni}^{2+}$  could be easily released from the surface of  $\text{NiMoO}_4$  precursor ( $K_{\text{sp}} = 6.3 \times 10^{-15}$ ) due to the acidic medium provided by  $\text{K}_3\text{Fe}(\text{CN})_6$  aqueous solution. Then, the dissolved  $\text{Ni}^{2+}$  ions tended to bind with  $[\text{Fe}(\text{CN})_6]^{3-}$  with the stronger coordination ( $K_{\text{sp}} = 1.8 \times 10^{-15}$ ) among solid-liquid interface, while such in-situ process led to scaffolding formation of PBA cubes on  $\text{NiMoO}_4$  nanorod [38,39]. Finally, the  $\text{Ni}^{2+}$  outward diffusion becomes dominant, and free  $\text{MoO}_4^{2-}$  dissolved in solution leading to the hollow nanorod array structure[40] as follows.



The formed PBA with surface atomic structure and unique nanostructures not only endowed ideal platform to synthesize high active heteroatom doped catalysts but also contributed to mass transfer of electrolytes and high specific area[39]. To verify the influence of structural variation, the  $\text{N}_2$  adsorption-desorption isotherms measurement was conducted via BET methods. As shown in Fig. 3b, the as-prepared  $\text{PBA@NiMoO}_4$  with hollow nanostructures was well indexed to Type IV isotherms[41], wherein the  $\text{PBA@NiMoO}_4$  was characterized with higher specific surface area ( $4.17 \text{ m}^2 \text{ g}^{-1}$ ) compared with  $\text{NiMoO}_4$  ( $2.40 \text{ m}^2 \text{ g}^{-1}$ ). The further treated Fe/P- $\text{NiMoO}_4$  after

phosphorization reaction also showed a well-preserved hollow morphology and mesopore with Type IV isotherms, which exhibited the highest specific surface area ( $8.97 \text{ m}^2 \text{ g}^{-1}$ ) leading to rich electrochemical active sites. Meanwhile, the aperture distribution of Fe/P- $\text{NiMoO}_4$  revealed the existence of mesopore, which mainly ranged from 10 to 20 nm (Fig. S6). The physical stretch force generated by the bubble evolution and detachment might cause negative effects on the mechanical stability of the catalyst[42]. Such unfavourable factors could be mitigated by engineering the mesoporous gas delivery path. As shown in Fig. 3c and d, the underwater gas-bubble contact angle was measured to be  $135.3^\circ$  for  $\text{PBA@NiMoO}_4$ , which was much larger than that of  $\text{NiMoO}_4$  ( $99.8^\circ$ ), demonstrating outstanding super aerophobic feature. Meanwhile, smaller gas bubbles for  $\text{PBA@NiMoO}_4$  and Fe, P- $\text{NiMoO}_4$  (Fig. S7) caused by the structural optimization could lead to enhanced aerophobic properties and rapid release of bubbles. The optimized gas bubble behavior enabled electrocatalysts efficient mass transfer between active sites and electrolyte, especially when applying at industrial current densities. Accordingly, the hollow interior could effectively maintain the stable operation during electrolysis under intense gaseous release especially high current density.

The surface chemical state of the prepared P- $\text{NiMoO}_4$  and Fe/P- $\text{NiMoO}_4$  were carried out by XPS. The full spectrum of Fe/P- $\text{NiMoO}_4$  indicated the presence of Mo, Ni, O, Fe, and P, consistent with the EDS result (Fig. 4a). The peak diffusion of Fe/P- $\text{NiMoO}_4$  might be caused by the successfully doping of Fe elements into  $\text{NiMoO}_4$ [43], compared with the spectra of P- $\text{NiMoO}_4$ . As can be seen from Mo 3d spectrum in Fig. 4b, the fitted curve indicated three chemical states of  $\text{Mo}^0$  (232.1 eV and 228.9 eV),  $\text{Mo}^{4+}$  (234.4 eV and 231.0 eV) and  $\text{Mo}^{6+}$  (236.3 eV and 233.3 eV)[44]. By comparing with the P- $\text{NiMoO}_4$ , it should be noted that  $\text{Mo}^0$ ,  $\text{Mo}^{4+}$  and  $\text{Mo}^{6+}$  of Fe/P- $\text{NiMoO}_4$  were positively shifted, confirming an electron redistribution around Mo. Moreover, the Ni 2p spectrum of Fe/P- $\text{NiMoO}_4$  indicated the presence of  $\text{Ni}^{2+}$  (875.3 eV and 857.6 eV) and other peaks at 881.0 eV and 862.7 eV could be attributed

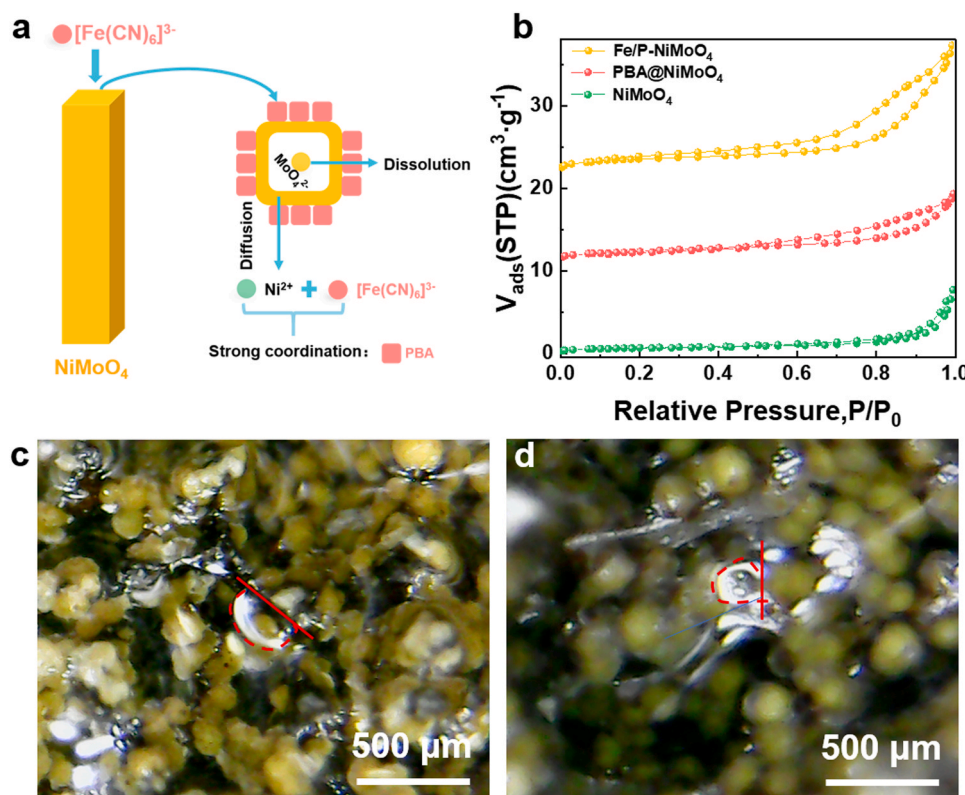


**Fig. 3.** (a) Schematic illustration of the formation of hollow  $\text{PBA@NiMoO}_4$ . (b)  $\text{N}_2$  adsorption-desorption isotherms of  $\text{NiMoO}_4$ ,  $\text{PBA@NiMoO}_4$  and Fe/P- $\text{NiMoO}_4$ . The photos of gas bubbles generated from (c)  $\text{NiMoO}_4$  and (d)  $\text{PBA@NiMoO}_4$ .

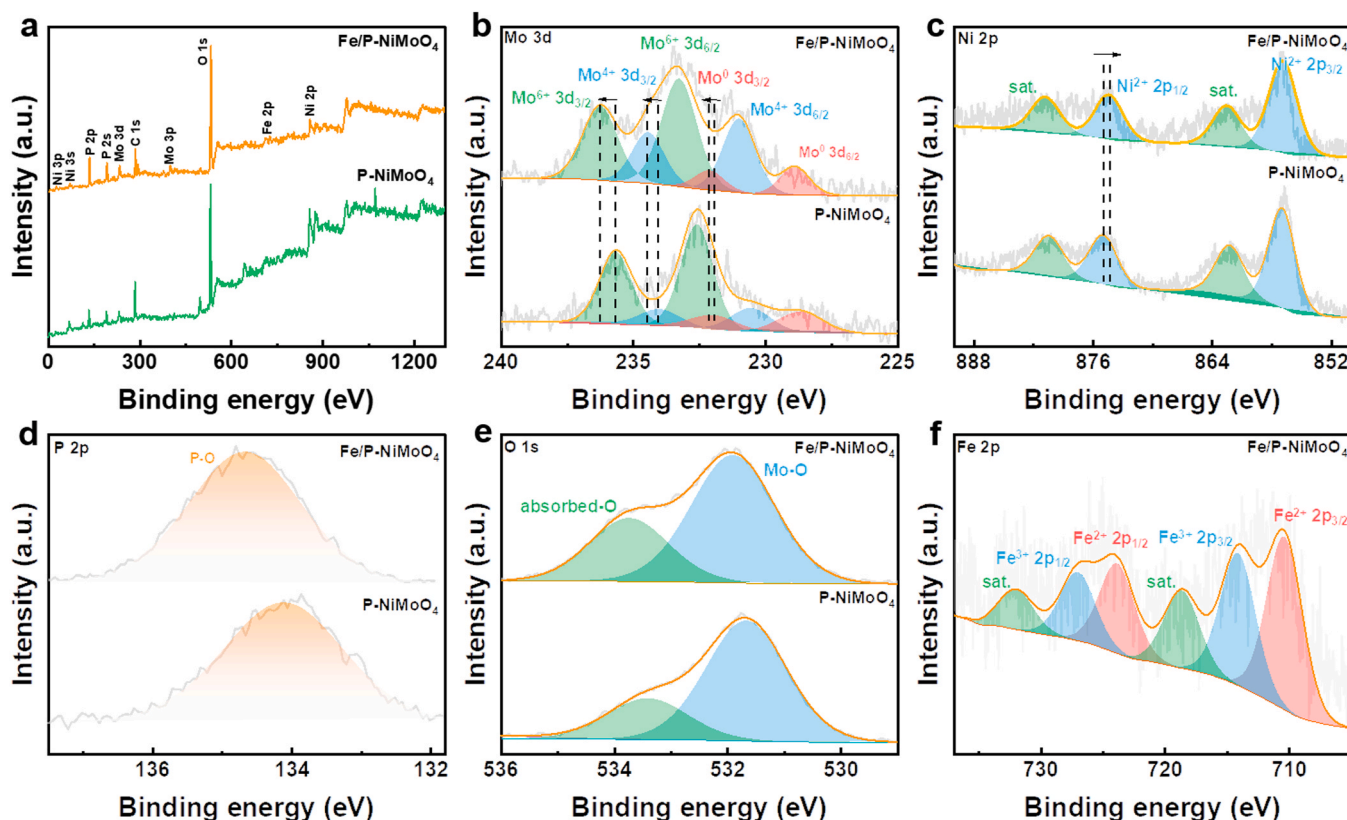


Fig. 4. (a) XPS full spectra spectra. (b) Mo 3d, (c) Ni 2p; (d) P 2p; (e) O 1 s and (f) Fe 2p spectra of Fe/P-NiMoO<sub>4</sub>.

to the satellite peaks[45] (Fig. 4c). In addition, the binding energy of Ni 2p in Fe/P-NiMoO<sub>4</sub> shifted negative compared with that of P-NiMoO<sub>4</sub> suggesting an electron redistribution at Ni sites[46]. As for P 2p XPS spectra in Fig. 4d, the formation of P-O species was well pointed to the peak of 134.7 eV, which might be due to the surface oxidation or phosphating procedure[47]. To analyze O species on the surface, the O 1 s spectrum of the Fe/P-NiMoO<sub>4</sub> could be deconvoluted into two peaks (Fig. 4e), which could be assigned to Mo-O (at 531.9 eV) and adsorbed-O (533.8 eV) species[37]. Fig. 4f displayed the XPS spectra of Fe 2p in Fe/P-NiMoO<sub>4</sub>, wherein the three pairs of peaks were deconvoluted at Fe<sup>2+</sup> (710.6 eV and 724.0 eV), Fe<sup>3+</sup> (714.3 eV and 727.2 eV) and satellite peaks (732.1 eV and 718.8 eV)[48]. The characterization results mentioned-above testified the hollow NiMoO<sub>4</sub> structure with effective doping by Fe and P elements[49].

### 3.2. Electrocatalytic performance for HER/OER and HzOR

The intrinsic electrochemical performance of as-prepared Fe/P-NiMoO<sub>4</sub> for HER and OER were investigated in alkaline seawater with a three-electrode system. To verify the bifunctional activity of Fe/P-NiMoO<sub>4</sub>, the state-of-the-art commercial Pt/C and RuO<sub>2</sub> were selected for comparison (HER and OER, respectively). First, the electrocatalytic activity was measured by LSV methods at 5 mV s<sup>-1</sup>, accompanied with P-NiMoO<sub>4</sub>, P-PBA, NF, Pt/C and RuO<sub>2</sub> as control catalysts. As shown in Fig. 5a, the hollow Fe/P-NiMoO<sub>4</sub> obtained superior catalytic HER and OER performances due to the low overpotentials (23 mV @ 10 mA cm<sup>-2</sup>; 213 mV @ 10 mA cm<sup>-2</sup> for HER and OER), which exceeded those of the P-NiMoO<sub>4</sub> (108 mV @ 10 mA cm<sup>-2</sup>; 216 @ 10 mA cm<sup>-2</sup>), P-PBA (179 mV @ 10 mA cm<sup>-2</sup>; 310 @ 10 mA cm<sup>-2</sup>), NF (284 mV @ 10 mA cm<sup>-2</sup>; 618 @ 10 mA cm<sup>-2</sup>), even commercial Pt/C (30 mV @ 10 mA cm<sup>-2</sup> for HER), RuO<sub>2</sub> (323 mV @ 10 mA cm<sup>-2</sup> for OER) and other reported advanced bifunctional catalysts (Fig. 5b and Table S1), which demonstrated the necessity of combining hollow

structure and Fe/P co-doping in enhancing the HER/OER performance. In addition, the kinetic parameter was illustrated as the  $\eta / \log(j)$ , which was driven from the polarization curves (Fig. S8). As depicted in Fig. 5c, Fe/P-NiMoO<sub>4</sub> owned the smallest Tafel slope (32.9 mV dec<sup>-1</sup> for HER; 46.8 mV dec<sup>-1</sup> for OER) in comparison with those of other catalysts, indicating its rapid reaction kinetics toward catalyzing HER/OER. Besides, abundant electrochemical active sites were also critical for electrocatalytic activity positively correlated to two-layer capacitance ( $C_{dl}$ ), which was further evaluated by cyclic voltammetry (CV) in alkaline seawater (Fig. S9 and Fig. S10). It could be clearly seen from Fig. 5c that the  $C_{dl}$  value of the Fe/P-NiMoO<sub>4</sub> sample was the highest (191.2 mF cm<sup>-2</sup> and 29.8 mF cm<sup>-2</sup> for HER and OER) than other catalysts, improving more reaction surface active area. To gain the interfacial charge transfer ability, electrochemical impedance spectroscopy (EIS) analysis of prepared samples were conducted as shown in Fig. 5d, wherein the Fe/P-NiMoO<sub>4</sub> owned the minimum charge transfer resistance ( $R_{ct}$ ) of 1.0  $\Omega$  and 0.92  $\Omega$  during HER and OER demonstrating superior charge transfer kinetics. The detailed values of as-prepared samples were mentioned in table S2, which was based on the Nyquist plots and fitted circuit diagram (Fig. S11). In addition, to get insight into the distinct merit of electrochemical performance by the turnover frequency (TOF), the polarization curves were normalized (Fig. 5e) with respected to the real number of active sites (Table S3), which was measured by the CV curves in phosphate buffer (pH=7) (Fig. S12). It should be noted that the Fe/P-NiMoO<sub>4</sub> possessed excellent inherent catalytic activity among controlled catalysts for HER and OER. Apart from the catalytic activity, the electrochemical stability was another crucial concern for the electrochemical performance, which could be tested by long-term chronopotentiometry measurement. As shown in Fig. 5f, the  $\eta$ - $t$  curve at constant high current density of 50, 250 and 500 mA cm<sup>-2</sup> displayed negligible decay within 150 h. On the other hand, the nanostructure of Fe/P-NiMoO<sub>4</sub> after stability test was observed by SEM image, wherein the hierarchical microsphere

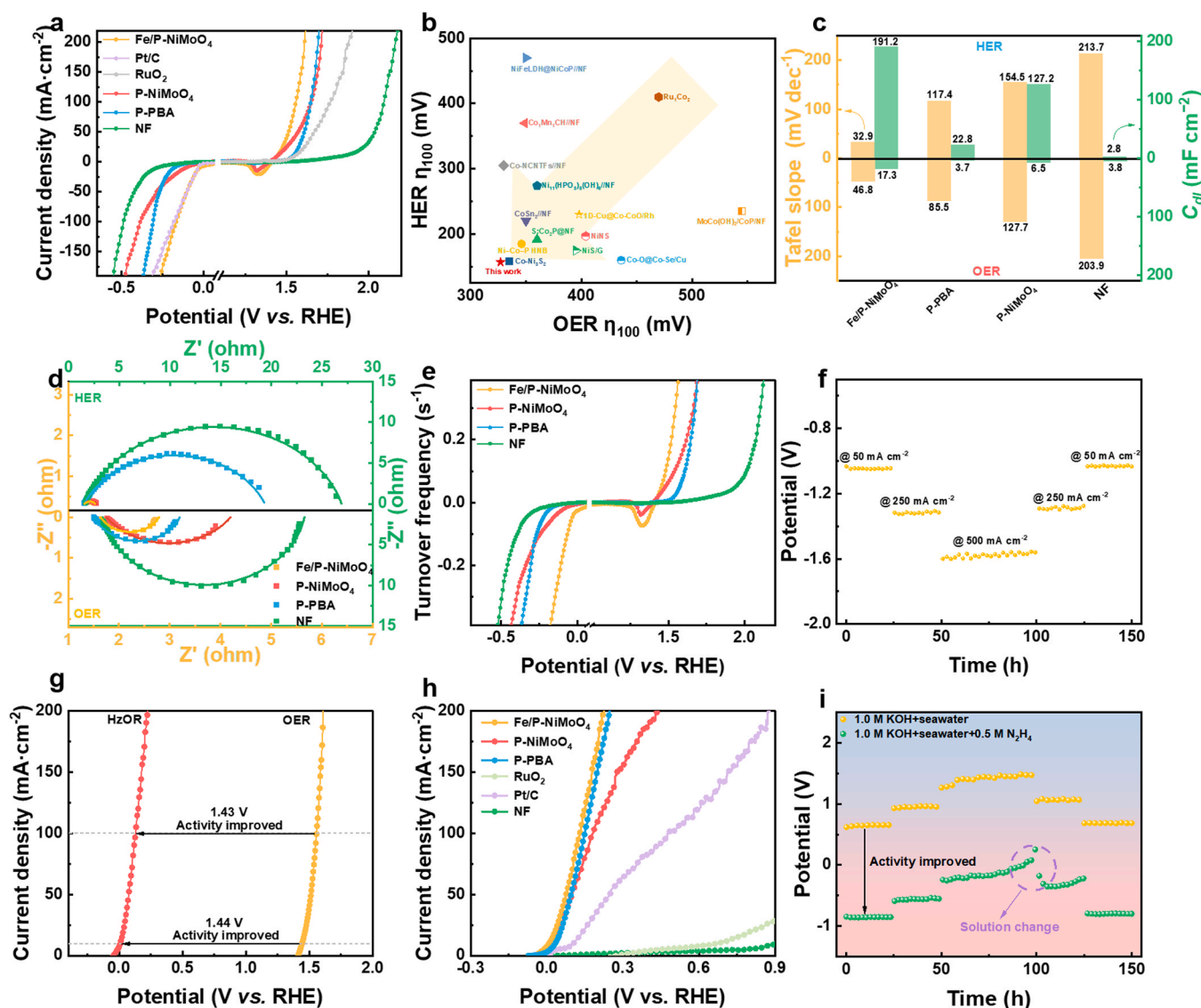


Fig. 5. (a) The polarization curves of prepared catalysts for HER and OER. (b) Comparison of the overpotentials at 100 mA cm<sup>-2</sup> for HER and OER with other reported catalysts. (c) The Tafel value and  $C_{dl}$  of all the prepared catalysts. (d) The EIS plots of various catalysts for HER and OER. (e) The TOFs plots of various catalysts for HER and OER. (f) Chronopotentiometry at 50, 250 and 500 mA cm<sup>-2</sup> of Fe/P-NiMoO<sub>4</sub> in alkaline seawater electrolyte for HER. (g) The voltage difference between HzOR and OER on Fe/P-NiMoO<sub>4</sub>. (h) The polarization curves of prepared catalysts for HzOR. (i) Chronopotentiometry at 50, 250 and 500 mA cm<sup>-2</sup> of Fe/P-NiMoO<sub>4</sub> in different electrolytes for OER and HzOR.

morphology was well maintained demonstrating the excellent operational stability in alkaline seawater for HER (Fig. S13).

Considering the commercial application for HER at large current density ( $> 1 \text{ A cm}^{-2}$ ), the process of OER would occurred with interference from CLER. The thermodynamically favourable HzOR reaction has been considered as an efficient method to offer an appropriate potential for avoiding the occurrence of CLER, which could be introduced without decrease of H<sub>2</sub> yielding efficiency during electrolysis. As depicted in Fig. 5g, the HzOR activity of Fe/P-NiMoO<sub>4</sub> was evaluated by LSV curves measured in alkaline seawater with 0.5 M hydrazine concentration. The electrode achieved current density of 10 mA cm<sup>-2</sup> and 100 mA cm<sup>-2</sup> only required ultralow potentials of 0.09 V and 0.13 V, respectively. In sharp contrast, the OER in N<sub>2</sub>H<sub>4</sub>-free alkaline seawater required 1.44 V and 1.55 V, respectively, for obtaining the same current density level, wherein the dramatic reduction was contributed to the low-cost hydrogen production. Meanwhile, compared with different scan rates from 5 to 50 mV s<sup>-1</sup> (Fig. S14), such LSVs exhibited negligible shift revealing rapid kinetics of Fe/P-NiMoO<sub>4</sub> occurred on the electrode-electrolyte-gas three-phase interface. The HzOR electrocatalytic activity

of the as-synthesized samples were also measured (Fig. 5h), wherein the Fe/P-NiMoO<sub>4</sub> required the lowest potentials and showed far excellent HzOR performance than commercial Pt/C and RuO<sub>2</sub>. As shown in Fig. S15, the Nyquist curves depicted that Fe/P-NiMoO<sub>4</sub> was characterized with smallest  $R_{ct}$  value, which was beneficial to reduce the energy barrier of electrode transfer. Besides, the HzOR intrinsic activity was probed by  $C_{dl}$ , which was further measured by CV at alkaline seawater with 0.5 M N<sub>2</sub>H<sub>4</sub> (Fig. S16). The calculated  $C_{dl}$  values of Fe/P-NiMoO<sub>4</sub> was determined to be largest 101.5 mF cm<sup>-2</sup> for HzOR, which was related to abundant electrochemically active surface area due to the 3D porous hollow structure. The durability of the Fe/P-NiMoO<sub>4</sub> as anode in different electrolytes were measured by long-term chronopotentiometry test at constant high current density of 50, 250 and 500 mA cm<sup>-2</sup> as shown in Fig. 5i. The  $v-t$  curves of the sample of Fe/P-NiMoO<sub>4</sub> remained basically unchanged during the continuous electrolysis for 150 h. Typically, for direct electrolysis of alkaline seawater with 0.5 M N<sub>2</sub>H<sub>4</sub>, the half-cell HzOR could reach a high current density of 500 mA cm<sup>-2</sup> below low voltage of -0.17 V, which was 1.59 V lower than direct electrolysis of alkaline seawater. It should be noted that the



nanostructure of Fe/P-NiMoO<sub>4</sub> was well maintained after stability test, wherein the hollow nanorods morphology could be observed by SEM image, demonstrating the excellent operational stability in alkaline seawater for OER and HzOR (Fig. S17).

### 3.3. Density function theory (DFT) calculation

To shed light on the effect of electronic modulations of Fe/P-NiMoO<sub>4</sub> on HER/OER and HzOR activity, the density functional theory (DFT) calculations were performed. According to the experiment results, the Fe/P co-doping NiMoO<sub>4</sub> (1 1 0) model was constructed and optimized, as shown in Fig. 6a. Meanwhile, the bonding of P-O was used to the model, which was confirmed by XPS results of P 2p spectra. In the preliminary trial, the Fe-NiMoO<sub>4</sub> model structure was conducted, wherein the Ni atom was replaced by Fe since the heteroatom Fe substituted Ni atom with the negative formation energy of  $-1.03$  eV

and Fe substituted Mo atom with the formation energy of  $1.46$  eV (Fig. S18). For comparison, the P-NiMoO<sub>4</sub> model structure was also conducted where O atom was replaced by P atom, as depicted in Fig. S19. First, the high electrochemical activity of Fe/P-NiMoO<sub>4</sub> could be attributed to the metallic property with enhanced electrical conductivity comparing with NiMoO<sub>4</sub> (Fig. S20), due to the increased DOS at Fermi level without evident gap[43]. In addition, the sequent doping of P and Fe atom for NiMoO<sub>4</sub> caused the upshifting of *d*-band centre towards the Fermi level ( $-4.861$  eV for NiMoO<sub>4</sub>,  $-4.771$  eV for P-NiMoO<sub>4</sub>,  $-4.618$  eV for Fe/P-NiMoO<sub>4</sub>), which increased the molecule and intermediates adsorption according to the *d*-band theory[50]. For verification, the detailed elementary reactions process for HER/OER activity origin of as-prepared sample were analyzed in theory. Due to the Fe, P co-doping, the electronic structure of active sites was modulated, which led to the appropriate H<sup>+</sup> adsorption. As shown in Fig. 6b, the calculated H adsorption Gibbs free energy ( $\Delta G_{H^*}$ ) on Fe site of

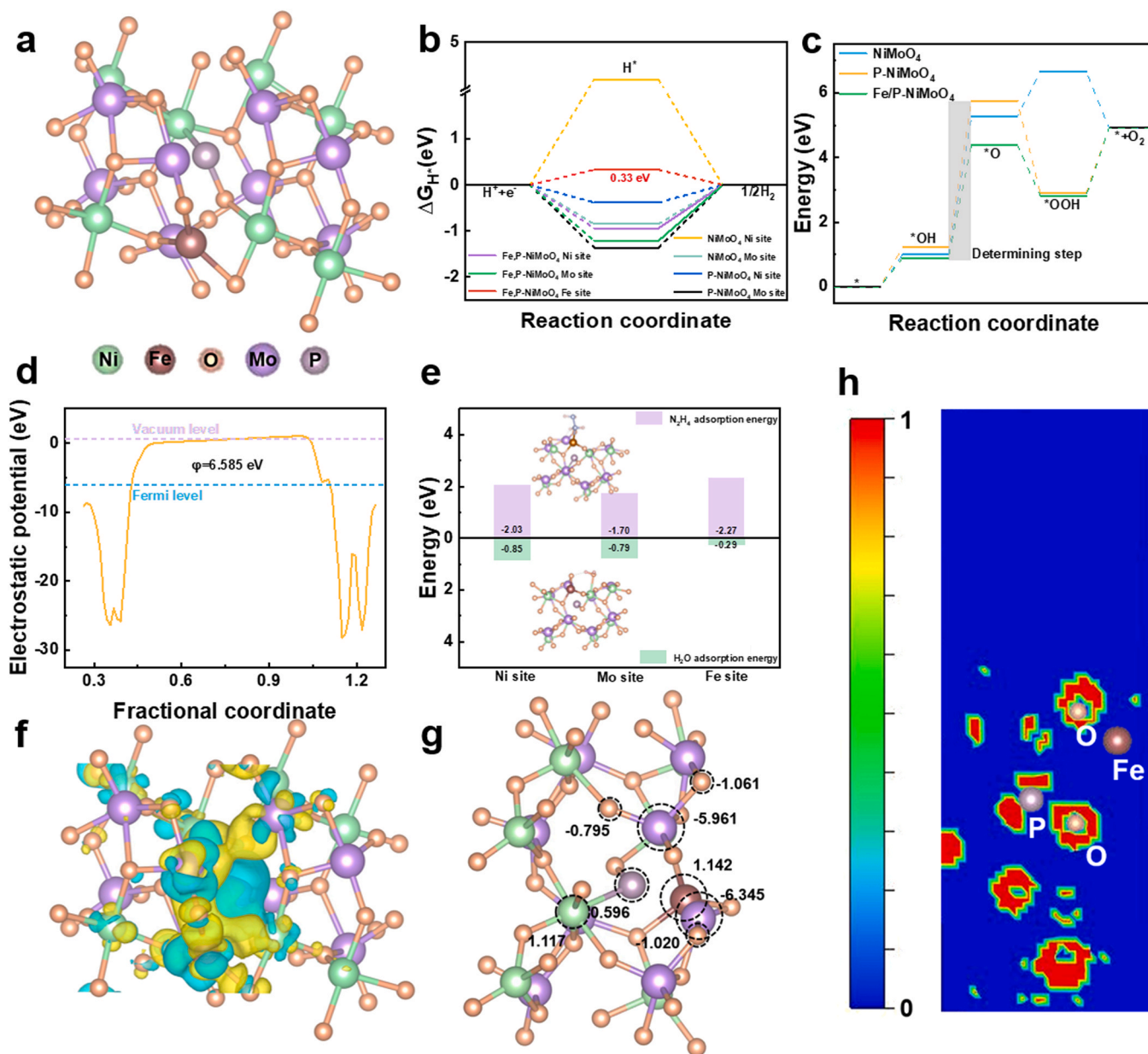


**Fig. 6.** (a) The structure model of Fe/P-NiMoO<sub>4</sub>. (b) The calculated Gibbs free energy diagram for the H adsorption of NiMoO<sub>4</sub>, P-NiMoO<sub>4</sub> and Fe/P-NiMoO<sub>4</sub>. (c) The calculated Gibbs free energy diagram for the intermediates adsorption of NiMoO<sub>4</sub>, P-NiMoO<sub>4</sub> and Fe/P-NiMoO<sub>4</sub>. (d) The computed work function of Fe/P-NiMoO<sub>4</sub>. (e) The N<sub>2</sub>H<sub>4</sub> and H<sub>2</sub>O adsorption energy of Fe/P-NiMoO<sub>4</sub>. (f) Charge density difference analysis for Fe/P-NiMoO<sub>4</sub>, wherein the cyan/yellow region was represented charge depletion/accumulation region, respectively. (g) Bader charge analysis for Fe/P-NiMoO<sub>4</sub>. (h) The electron-localization function of Fe/P-NiMoO<sub>4</sub>.

Fe/P-NiMoO<sub>4</sub> much approached the ideal  $\Delta G_{H^+}$  of 0.33 eV, indicating the balance of adsorption and dissociation processes of the hydrogen intermediate. Meanwhile, the  $\Delta G$  of the detailed elementary reactions process for OER was also obtained as revealed in Fig. 6c and Table S4. Notably, it was inferred that the induce of heteroatoms was more favourable to the reaction with the intermediates among OER process comparing to the pure NiMoO<sub>4</sub>, in which the rate determining step was the  $\text{OH}^* \rightarrow \text{O}^*$  step for all prepared samples. Obviously, the  $\Delta G$  value of Fe/P-NiMoO<sub>4</sub> (3.50 eV) was much smaller than that of other catalysts (Table S4), thus indicating to the reduced energy barrier for the OER process. Moreover, the corresponding work function was calculated to evaluate the electron migration as shown in Fig. 6d and Fig. S21. The work function value (6.585 eV) of Fe/P-NiMoO<sub>4</sub> was lower than that of NiMoO<sub>4</sub> (6.993 eV), which meant less energy to migrate free electrons among Fe/P-NiMoO<sub>4</sub> during the electrochemical reaction. The H<sub>2</sub>O and N<sub>2</sub>H<sub>4</sub> molecules adsorption behaviour of different sites (Fe, Mo, Ni) on Fe/P-NiMoO<sub>4</sub> model were investigated (Fig. S22 and Fig. S23). As shown

in Fig. 6e, the adsorption energies on these models were compared, in which the H<sub>2</sub>O molecules was priority to adsorb on Ni sites and N<sub>2</sub>H<sub>4</sub> molecules was priority to adsorb on Fe sites in the initial period. The large adsorption energy corroborated rapid activation of adsorbed molecules, which has been considered to be beneficial for the electrocatalytic process. The diagram of charge density difference in Fig. 6f exhibited charge concentration enhanced area, which was generated by the electron localization phenomenon of Fe/P co-doping. Meanwhile, further support could be provided by the electron-localization function of Fe/P-NiMoO<sub>4</sub> of (−19.6, −1, −15.7) plane in Fig. 6h. The Bader charge analysis was applied to calculated the differential charge density at the interface after Fe/P doping (Fig. 6g). Typically, compared with simplex NiMoO<sub>4</sub> model (+1.273 e) (Fig. S24a), the Ni atoms (+1.117 e) around P atom exhibited electron-rich states after the introduction of P dopant (Fig. 6f), since the lower electronegativity of P than O, thus leading a higher electron cloud density for Ni atom [51]. Similarly, compared with simplex NiMoO<sub>4</sub> model (+1.196 e) (Fig. S24b), the Fe

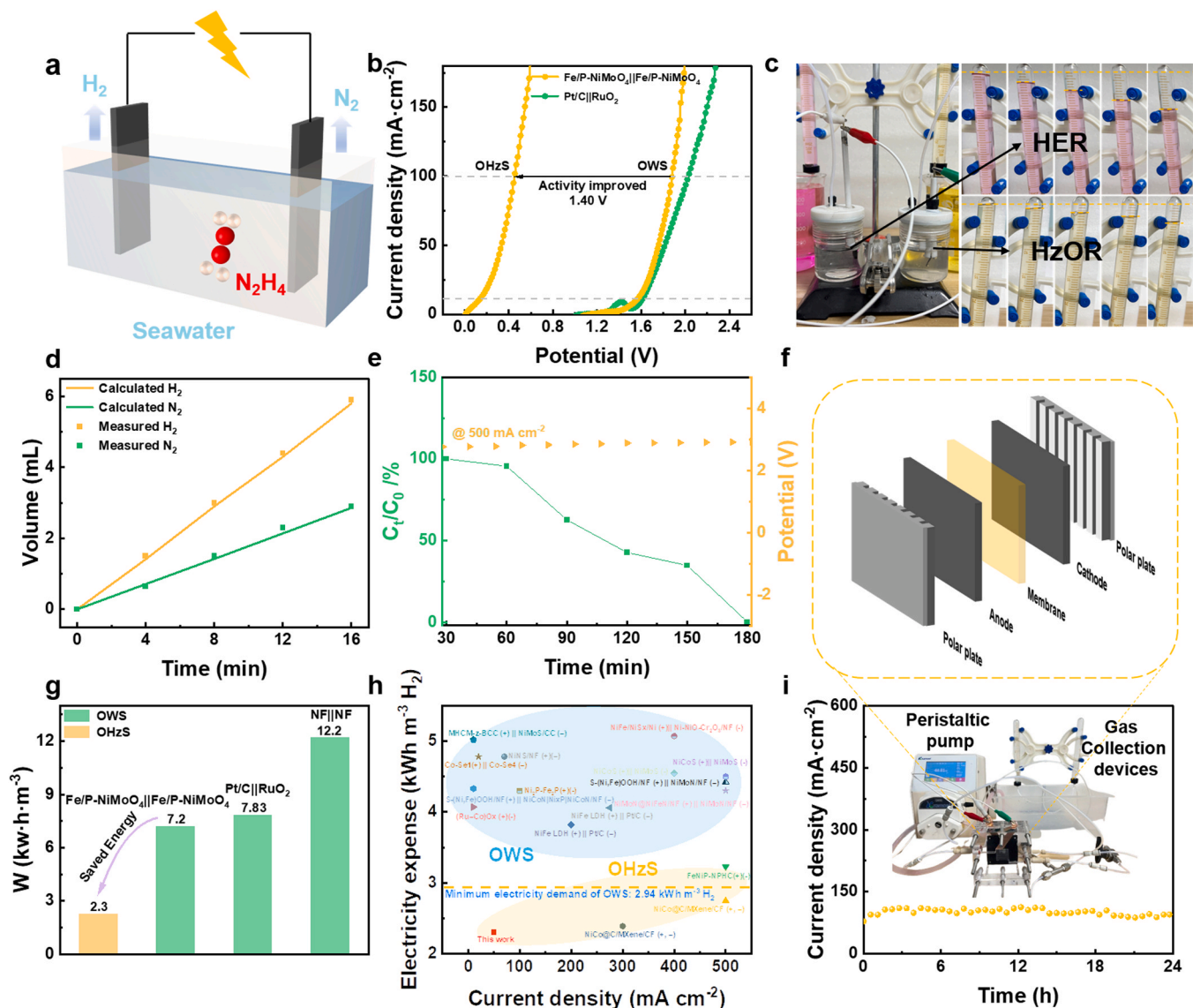


**Fig. 7.** (a) Schematic illustration of overall hydrazine splitting. (b) The polarization curves of Fe/P-NiMoO<sub>4</sub> // Fe/P-NiMoO<sub>4</sub> and Pt/C // RuO<sub>2</sub> in different electrolytes. (c) The photos for calculating the Faraday efficiency. (d) The amounts of theoretical and generated gases (H<sub>2</sub> and N<sub>2</sub>) in alkaline seawater with 0.5 M N<sub>2</sub>H<sub>4</sub>. (e) The activity and stability of two electrodes system for hydrazine degradation at 500 mA cm<sup>-2</sup>. (f) Schematic illustration of MEA reactor. (g) A comparison of energy consumption of overall hydrazine splitting and overall seawater splitting for various samples. (h) A comparison of this work and reported seawater splitting electrolyzer (blue region) and hydrazine splitting electrolyzer (yellow region). (i) Chronoamperometry test of Fe/P-NiMoO<sub>4</sub> // Fe/P-NiMoO<sub>4</sub> in alkaline seawater electrolyte with 0.5 M N<sub>2</sub>H<sub>4</sub> (~100 mA cm<sup>-2</sup>), wherein the inset photo was the assembled MEA system.

atoms (+1.142 e) (Fig. 6g) around P atom exhibited relatively electron-rich states. Such electrons accumulation on molecules adsorption sites was beneficial to the activation of reactants thus causing optimized electrochemical kinetics[43], which further revealed the important modulations generated by Fe/P doping.

### 3.4. Electrocatalytic performance of hybrid seawater electrolyzer

Encouraged by the favourable electrochemical performance, a two-electrode configuration was fabricated with Fe/P-NiMoO<sub>4</sub> working as both anode and cathode (Fig. 7a), which was applied for hybrid seawater splitting coupling hydrazine oxidation (HzOR). The combination of commercial Pt/C and RuO<sub>2</sub> was used as comparison. First, the LSV curves of Fe/P-NiMoO<sub>4</sub> // Fe/P-NiMoO<sub>4</sub> electrolyzer was measured in alkaline seawater (Fig. 7b), the applied potentials to reach 10 mA cm<sup>-2</sup> and 100 mA cm<sup>-2</sup> were 1.55 V and 1.88 V, which was smaller than that of Pt/C // RuO<sub>2</sub> (1.60 V and 2.03 V, respectively), indicating the potential of Fe/P-NiMoO<sub>4</sub> as high-effective electrocatalyst. Meanwhile, to demonstrate the activity and stability of Fe/P-NiMoO<sub>4</sub> among large-scale industrial hydrogen production under industrial level current density, the evaluation of a two-electrode cell under larger current density has been employed. As shown in Fig. S25, the applied potentials to reach 500 mA cm<sup>-2</sup> and 1000 mA cm<sup>-2</sup> were 1.95 V and 2.17 V and the *v-t* curves of the system remained basically unchanged during the continuous electrolysis for 100 h among 500 mA cm<sup>-2</sup>. Then, as shown in Fig. 7b, after introducing HzOR for hydrogen production, the cell voltage was decreased to 0.13 V and 0.45 V at current density of 10 mA cm<sup>-2</sup> and 100 mA cm<sup>-2</sup>, respectively, wherein the activity far excelled the OWS (voltage gap: 1.40 V). In addition, the Faradaic efficiency of two-electrode cell containing Fe/P-NiMoO<sub>4</sub> was gained by drainage method (Fig. 7c). It should be noted that the volume of collected gas approached the theoretical thresholds, which were determined to be ~100% for HER and HzOR reaction, thus demonstrating the superior reactive selectivity (Fig. 7d). Similarly, the Faradaic efficiency of two-electrode cell without hydrazine was also measured to be ~100% for HER and OER (Fig. S26). Apart from the provided thermodynamic advantages by Fe/P-NiMoO<sub>4</sub>, the HzOR without complex separation and extra added oxidizing agent has been considered as effective method[23]. As shown in Fig. 7e, it allowed the toxic hydrazine to be removed ~100% within 180 mins at a constant current density, which could be tested by concentration-absorbance curve via the Watt and Chrisp method (Fig. S27). Besides, a scale-up MEA reactor was conducted to confirm the feasibility of the industrial application (Fig. 7f), in which the Fe/P-NiMoO<sub>4</sub> electrodes were applied as cathode/anode and divided by alkaline exchange membrane in different electrolytes to prevented the confusion of gases. In addition, the peristaltic pump and gas collection devices was applied in the MEA system, wherein the amount of gaseous products measuring with the water drainage method was used for the calculation of energy consumption. As shown in Fig. 7g, the introduction of Fe/P-NiMoO<sub>4</sub> visually decreased the energy consumption (7.2 kW h m<sup>-3</sup>) of MEA reactor at 150 mA cm<sup>-2</sup> in alkaline seawater, comparing with Pt/C // RuO<sub>2</sub> (7.8 kW h m<sup>-3</sup>) and NF // NF (12.2 kW h m<sup>-3</sup>), indicating the superiority of commercial application. Moreover, replacing OER with HzOR process allowed for energy-saving hydrogen production among MEA reactor. In addition, it was worth noting that Fe/P-NiMoO<sub>4</sub> // Fe/P-NiMoO<sub>4</sub> proceeded negligible shift of LSV curves with different flow rates from 7.5 to 22.5 mL min<sup>-1</sup>, while the Pt/C // RuO<sub>2</sub> and NF // NF systems exhibited decreased OWS performance at lower flow rate, showing optimized kinetic on electrode-electrolyte-gas triple-phase interface on Fe/P-NiMoO<sub>4</sub> (Fig. S28). In alkaline seawater with 0.5 M hydrazine, the energy consumption at 150 mA cm<sup>-2</sup> only required ultralow 2.3 kW h m<sup>-3</sup>, which with low electricity expense provided the feasibility to realize large-scale hydrogen production system. The electrochemical performance of such MEA reactor with OWS and OH<sub>2</sub>S also far excelled the reported advanced electrolyzers in regard to the energy

efficiency (Fig. 7f and Table S5). Finally, Fig. 7i showed the good long-term stability of the Fe/P-NiMoO<sub>4</sub> couple in MEA reactor for 24 h to maintain ~100 mA cm<sup>-2</sup> indicating the feasibility in practical application.

### 3.5. Chloride corrosion resistance analysis

Chloride corrosion, as a challenging issue, should be addressed for long-term and industrial water electrolysis. In this work, to better reflect the corrosion resistance performance, the Fe/P-NiMoO<sub>4</sub> was firstly immersed in natural seawater for 30 days. It should be noted that the Fe/P-NiMoO<sub>4</sub> presented a well-maintained hierarchical microsphere array structure without obvious structural collapse, as shown in Fig. S29. In addition, corresponding corrosion polarization curves of as-prepared samples were measured in natural seawater to show the anti-corrosion capability. As shown in Fig. 8a, the Fe/P-NiMoO<sub>4</sub> exhibited the highest corrosion potential (-0.703 V vs. SCE), implying that Fe/P-NiMoO<sub>4</sub> experience a best corrosion resistance in seawater among all the samples. To gain deep insights into the corrosion resistance of Fe/P-NiMoO<sub>4</sub>, the Zeta potential were further measured as shown in Fig. 8b, which could effectively reflect the ability to repel negatively charged Cl<sup>-</sup> ions [52]. Compared with that of NiMoO<sub>4</sub> (-1.40 mV) and PBA@NiMoO<sub>4</sub> (-1.66 mV), the Fe/P-NiMoO<sub>4</sub> exhibited the lowest Zeta potential (-7.43 mV) indicating the enhanced chlorine-repelling ability. In order to exclude the effect caused by catalyst transformation, the zeta potentials were measured for the Fe/P-NiMoO<sub>4</sub> after the different reactions, and the results showed that the catalyst still has negative Zeta potential, which revealed that Fe/P-NiMoO<sub>4</sub> has a good chloride corrosion resistance (Fig. S30). Finally, to confirm the concern of probable hypochlorite production on anode, a colourimetric method was conducted via UV-vis spectrophotometer, which allowed N, N-diethyl-p-phenylenediamine (DPD) oxidation with visible colour variation as depicted in Fig. S31. For direct electrolysis of alkaline seawater electrolyzer (ASE), the anolyte among Fe/P-NiMoO<sub>4</sub> // Fe/P-NiMoO<sub>4</sub> system showed low ClO<sup>-</sup> concentration (0.104% for 36 h and 0.144% for 46 h) during continuous electrolysis, which much lower than that of NF // NF in ASE, indicating low-concentration ClO<sup>-</sup> corrosion (Fig. S32 and Fig. S33). Meanwhile, as sharp contrast, no ClO<sup>-</sup> generation was detected for the anolyte among Fe/P-NiMoO<sub>4</sub> // Fe/P-NiMoO<sub>4</sub> system of hybrid seawater electrolyzer (HSE), which was attributed to the ultralow cell voltage at 100 mA cm<sup>-2</sup> disregarding anodic corrosion and Cl<sup>-</sup> crossover. These results suggested that the introduction of Fe/P-NiMoO<sub>4</sub> was critical to maintain stable electrolysis operation for hybrid seawater splitting in terms of chloride corrosion resistance.

## 4. Conclusion

In summary, we successfully constructed integrated hollow NiMoO<sub>4</sub> nanorod with Fe/P dual-doping on Ni foam substrate as highly efficient trifunctional electrocatalyst, which achieved remarkable electrochemical activity toward HER/OER and HzOR in alkaline seawater. Such hollow nanostructure endowed catalysts with rich electrochemically active sites and enhanced mass diffusion kinetic. Benefitting from the coupling effect of Fe, P co-doping as well as unique hollow structure, the as-synthesized Fe/P-NiMoO<sub>4</sub> exhibited superior HER (23 mV @ 10 mA cm<sup>-2</sup>) and OER (213 mV @ 10 mA cm<sup>-2</sup>) activity compared with state-of-the-art electrocatalysts. Meanwhile, the introduction of Fe/P-NiMoO<sub>4</sub> among hybrid seawater electrolysis realized energy-saving seawater splitting without hypochlorite production in alkaline seawater/0.5 M N<sub>2</sub>H<sub>4</sub> electrolyte. Impressively, the prepared Fe/P-NiMoO<sub>4</sub> also has good long-term stability even for industrial current density of 500 mA cm<sup>-2</sup> and obtained ~100% Faradaic efficiency for OWS and OH<sub>2</sub>S. MEA electrochemical reactor using Fe/P-NiMoO<sub>4</sub> in alkaline seawater/0.5 M N<sub>2</sub>H<sub>4</sub> only required energy consumption of 2.3 kW h m<sup>-3</sup> for OH<sub>2</sub>S, indicating the remarkable advantage among overall seawater splitting and hydrazine splitting. Finally, in-depth DFT



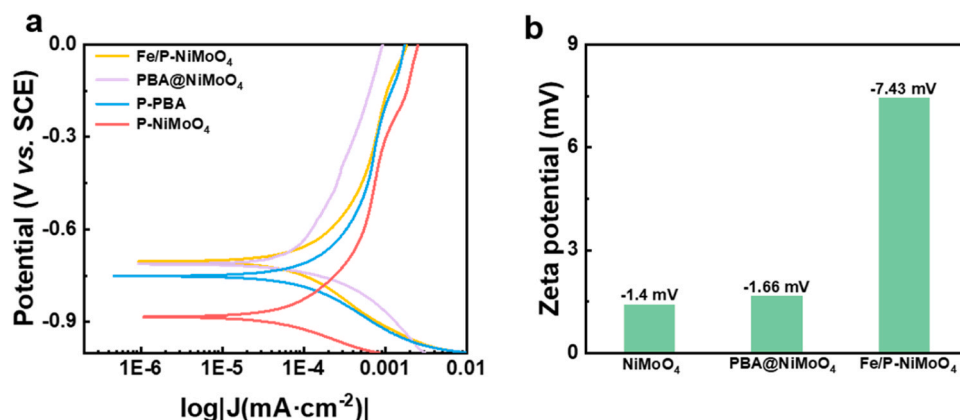


Fig. 8. (a) Corrosion polarization curves of the as-prepared samples. (b) Zeta potentials of NiMoO<sub>4</sub>, PBA@NiMoO<sub>4</sub> and Fe/P-NiMoO<sub>4</sub>.

calculation clarified the outstanding electrochemical activity, wherein the Fe/P doping could not only lead to metallic property with enhanced electrical conductivity but also modulate *d*-band center causing enhanced adsorption between molecule and intermediates. Hence, this work offered rational design of electrocatalyst and energy-saving strategy for high effective hydrogen production among carbon-free system, which was potential to realize contamination-free environment.

#### Declaration of Competing Interest

The authors declare that they have no known competing financial interests or personal relationships that could have appeared to influence the work reported in this paper.

#### Data Availability

Data will be made available on request.

#### Acknowledgements

This work was financially supported by Shandong Provincial Natural Science Foundation (Grant No.: ZR2021QB056), Taishan Scholars Foundation of Shandong Province (No.: tsqn201909058), and the Fundamental Research Funds for the Central Universities (No.: 202364004, 202261014).

#### Appendix A. Supporting information

Supplementary data associated with this article can be found in the online version at [doi:10.1016/j.apcatb.2024.123805](https://doi.org/10.1016/j.apcatb.2024.123805).

#### References

- [1] S. Chu, A.Jn Majumdar, Opportunities and challenges for a sustainable energy future, *Nature* 488 (2012) 294–303.
- [2] J. Sun, Z. Zhang, X. Meng, Low-Pt supported on MOF-derived Ni(OH)<sub>2</sub> with highly-efficient electrocatalytic seawater splitting at high current density, *Appl. Catal. B: Environ.* 331 (2023) 122703–122713.
- [3] E. Murugan, S. Govindaraju, S. Santhoshkumar, Hydrothermal synthesis, characterization and electrochemical behavior of NiMoO<sub>4</sub> nanoflower and NiMoO<sub>4</sub>/rGO nanocomposite for high-performance supercapacitors, *Electrochim. Acta* 392 (2021).
- [4] S.P. Ratnayake, M. Mantilaka, C. Sandaruwan, D. Dahanayake, E. Murugan, S. Kumar, G.A.J. Amaratunga, K.M.N. de Silva, Carbon quantum dots-decorated nano-zirconia: A highly efficient photocatalyst, *Appl. Catal. A: Gen.* 570 (2019) 23–30.
- [5] X. Liu, X. Jin, J. Yan, S. Fan, Y. Wang, D. Astruc, “On-off” control for on-demand H<sub>2</sub> evolution upon Si-H bond hydrolysis: A combined experimental and theoretical study, *Appl. Catal. B: Environ.* 324 (2023).
- [6] W. Huang, F. Xu, D.S. Li, D. Astruc, X. Liu, “On-off” switch for H<sub>2</sub> and O<sub>2</sub> generation from HCOOH resp. H<sub>2</sub>O<sub>2</sub>, *Carbon Energy* 5 (2022).
- [7] Z. Zhao, J. Sun, Z. Li, X. Xu, Z. Zhang, C. Li, L. Wang, X. Meng, Rapid synthesis of efficient Mo-based electrocatalyst for the hydrogen evolution reaction in alkaline seawater with 11.28% solar-to-hydrogen efficiency, *J. Mater. Chem. A* 11 (2023) 10346–10359.
- [8] Y. Zhu, J. Zhang, Q. Qian, Y. Li, Z. Li, Y. Liu, C. Xiao, G. Zhang, Y. Xie, Dual nanoislands on Ni/C hybrid nanosheet activate superior hydrazine oxidation-assisted high-efficiency H<sub>2</sub> production, *Angew. Chem. Int. Ed. Engl.* 61 (2022) e202113082.
- [9] Z. Li, W. Wang, Q. Qian, Y. Zhu, Y. Feng, Y. Zhang, H. Zhang, M. Cheng, G. Zhang, Magic hybrid structure as multifunctional electrocatalyst surpassing benchmark Pt/C enables practical hydrazine fuel cell integrated with energy-saving H<sub>2</sub> production, *eScience* 2 (2022) 416–427.
- [10] Q. Yu, X. Liu, G. Liu, X. Wang, Z. Li, B. Li, Z. Wu, L. Wang, Constructing three-phase heterojunction with 1D/3D hierarchical structure as efficient trifunctional electrocatalyst in alkaline seawater, *Adv. Funct. Mater.* 32 (2022) 2205767–2205777.
- [11] J. Sun, S. Qin, Z. Zhao, Z. Zhang, X. Meng, Rapid carbothermal shocking fabrication of iron-incorporated molybdenum oxide with heterogeneous spin states for enhanced overall water/seawater splitting, *Mater. Horiz.* (2023).
- [12] J. Sun, Z. Zhao, Z. Li, Z. Zhang, R. Zhang, X. Meng, Ultrafast carbothermal shocking fabrication of cation vacancy-rich Mo doped Ru nanoparticles on carbon nanotubes for high-performance water/seawater electrolysis, *J. Mater. Chem. A* 11 (2023) 22430–22440.
- [13] J. Sun, G. Ren, S. Qin, Z. Zhao, Z. Li, Z. Zhang, C. Li, X. Meng, Reconstruction Co-O-Mo in amorphous-crystalline MoO<sub>x</sub>/Co(OH)<sub>2</sub> interface for industry-level active and stable electrocatalytic seawater hydrogen evolution, *Nano Energy* (2023).
- [14] Z. Li, X. He, Q. Qian, Y. Zhu, Y. Feng, W. Wan, G. Zhang, Active site implantation for Ni(OH)<sub>2</sub> nanowire network achieves superior hybrid seawater electrolysis at 1 A cm<sup>-2</sup> with record-low cell voltage, *Adv. Funct. Mater.* 33 (2023).
- [15] M. Chen, N. Kitiphatpiboon, C. Feng, A. Abudula, Y. Ma, G. Guan, Recent progress in transition-metal-oxide-based electrocatalysts for the oxygen evolution reaction in natural seawater splitting: a critical review, *eScience* 3 (2023).
- [16] Y. Song, M. Sun, S. Zhang, X. Zhang, P. Yi, J. Liu, B. Huang, M. Huang, L. Zhang, Alleviating the work function of Vein-like Co<sub>3</sub>P by Cr doping for enhanced seawater electrolysis, *Adv. Funct. Mater.* (2023) 2214081–2214091.
- [17] Z. Zhao, J. Sun, X. Meng, Recent advances in transition metal-based electrocatalysts for seawater electrolysis, *Int. J. Energy Res.* 46 (2022) 17952–17975.
- [18] Z. Zhao, J. Sun, X. Li, Z. Zhang, X. Meng, Joule heating synthesis of NiFe alloy/MoO<sub>2</sub> and in-situ transformed (Ni,Fe)OOH/MoO<sub>2</sub> heterostructure as effective complementary electrocatalysts for overall splitting in alkaline seawater, *Appl. Catal. B: Environ.* 340 (2024).
- [19] Z. Zhao, J. Sun, Z. Li, X. Xu, Z. Zhang, C. Li, L. Wang, X. Meng, Rapid synthesis of efficient Mo-based electrocatalyst for the hydrogen evolution reaction in alkaline seawater with 11.28% solar-to-hydrogen efficiency, *J. Mater. Chem. A* 11 (2023) 10346–10359.
- [20] S. Drespf, F. Dionigi, M. Klingenhof, P. Strasser, Direct electrolytic splitting of seawater: opportunities and challenges, *ACS Energy Lett.* 4 (2019) 933–942.
- [21] S. Drespf, T.N. Thanh, M. Klingenhof, S. Brückner, P. Hauke, P.J.E. Strasser, E. Science, Efficient direct seawater electrolyzers using selective alkaline NiFe-LDH as OER catalyst in asymmetric electrolyte feeds, *Energy Environ. Sci.* 13 (2020) 1725–1729.
- [22] X. Xu, H.C. Chen, L. Li, M. Humayun, X. Zhang, H. Sun, D.P. Debecker, W. Zhang, L. Dai, C. Wang, Leveraging metal nodes in Metal-organic frameworks for advanced anodic hydrazine oxidation assisted seawater splitting, *ACS Nano* (2023) 10906–10917.
- [23] F. Sun, J. Qin, Z. Wang, M. Yu, X. Wu, X. Sun, J. Qiu, Energy-saving hydrogen production by chlorine-free hybrid seawater splitting coupling hydrazine degradation, *Nat. Commun.* 12 (2021) 4182.
- [24] T. Wang, X. Cao, L. Jiao, Progress in hydrogen production coupled with electrochemical oxidation of small molecules, *Angew. Chem.* 61 (2022) e202213328.

- [25] H. Beitollahi, M.A. Khalilzadeh, S. Tajik, M. Safaei, K. Zhang, H.W. Jang, M.J. Ao Shokouhimehr, Recent advances in applications of voltammetric sensors modified with ferrocene and its derivatives, *ACS Omega* 5 (2020) 2049–2059.
- [26] C. Ye, J. Liu, Q. Zhang, X. Jin, Y. Zhao, Z. Pan, G. Chen, Y. Qiu, D. Ye, L. Gu, G.I. N. Waterhouse, L. Guo, S. Yang, Activating metal oxides nanocatalysts for electrocatalytic water oxidation by Quenching-induced Near-surface metal atom functionality, *J. Am. Chem. Soc.* 143 (2021) 14169–14177.
- [27] D. Guo, Y. Luo, X. Yu, Q. Li, T.J.N.E. Wang, High performance NiMoO<sub>4</sub> nanowires supported on carbon cloth as advanced electrodes for symmetric supercapacitors, *Nano Energy* 8 (2014) 174–182.
- [28] A. Muthurasu, A.P. Tiwari, K. Chhetri, B. Dahal, H.Y. Kim, Construction of iron doped cobalt- vanadate- cobalt oxide with metal-organic framework oriented nanoflakes for portable rechargeable zinc-air batteries powered total water splitting, *Nano Energy* 88 (2021).
- [29] R. Farhat, J. Dhainy, L.I. Halaoui, OER catalysis at activated and codeposited NiFe-Oxo/hydroxide thin films is due to postdeposition surface-fe and is not sustainable without Fe in solution, *ACS Catal.* 10 (2019) 20–35.
- [30] J. Chang, G. Wang, Z. Yang, B. Li, Q. Wang, R. Kuliev, N. Orlovskaya, M. Gu, Y. Du, G. Wang, Y. Yang, Dual-doping and synergism toward high-performance seawater electrolysis, *Adv. Mater.* 33 (2021) e2101425.
- [31] P. Yang, M. Ren, C. Jin, H. Xing, Facile synthesis of N and P Co-Doped NiMoO<sub>4</sub> hollow nanowires and electrochemical deposition of NiFe-layered double hydroxide for boosting overall seawater splitting, *J. Electrochem. Soc.* 169 (2022).
- [32] Y. Liu, J. Zhang, Y. Li, Q. Qian, Z. Li, Y. Zhu, G. Zhang, Manipulating dehydrogenation kinetics through dual-doping Co<sub>3</sub>N electrode enables highly efficient hydrazine oxidation assisting self-powered H<sub>2</sub> production, *Nat. Commun.* 11 (2020) 1853–1866.
- [33] J. Nai, X.W.D. Lou, Hollow structures based on prussian blue and its analogs for electrochemical energy storage and conversion, *Adv. Mater.* 31 (2019) 1706825–1706845.
- [34] A.S. Botana, M.R. Norman, Electronic structure and magnetism of transition metal dihalides: bulk to monolayer, *Phys. Rev. Mater.* 3 (2019) 044001–044008.
- [35] J. Tao, J.P. Perdew, H. Tang, C. Shahi, Origin of the size-dependence of the equilibrium van der Waals binding between nanostructures, *J. Chem. Phys.* 148 (2018) 074110–074117.
- [36] L. Chaput, P. Pécheur, H. Scherrer, Thermopower, Hall tensor, and relaxation time approximation for elemental zinc, *Phys. Rev. B* 75 (2007) 045116–045121.
- [37] W. Shi, J. Zhu, L. Gong, D. Feng, Q. Ma, J. Yu, H. Tang, Y. Zhao, S. Mu, Fe-Incorporated Ni/MoO<sub>2</sub> hollow heterostructure nanorod arrays for High-efficiency overall water splitting in alkaline and seawater media, *Small* 18 (2022) 2205683–2205692.
- [38] Y. Wang, J. Ma, J. Wang, S. Chen, H. Wang, J. Zhang, Interfacial scaffolding preparation of hierarchical PBA-Based derivative electrocatalysts for efficient water splitting, *Adv. Energy Mater.* 9 (2019).
- [39] Y. Wang, S. Zhao, Y. Zhu, R. Qiu, T. Gengenbach, Y. Liu, L. Zu, H. Mao, H. Wang, J. Tang, D. Zhao, C. Selomulya, Three-dimensional hierarchical porous nanotubes derived from Metal-organic frameworks for highly efficient overall water splitting, *iScience* 23 (2020) 100761–100774.
- [40] Z.-Y. Yu, Y. Duan, J.-D. Liu, Y. Chen, X.-K. Liu, W. Liu, T. Ma, Y. Li, X.-S. Zheng, T.J. N.C. Yao, Unconventional CN vacancies suppress iron-leaching in Prussian blue analogue pre-catalyst for boosted oxygen evolution catalysis, *Nat. Commun.* 10 (2019) 2799–2808.
- [41] M. Thommes, K. Kaneko, A.V. Neimark, J.P. Olivier, F. Rodriguez-Reinoso, J. Rouquerol, K.S.W. Sing, Physisorption of gases, with special reference to the evaluation of surface area and pore size distribution (IUPAC Technical Report), *Pure Appl. Chem.* 87 (2015) 1051–1069.
- [42] Q. Song, Z. Xue, C. Liu, X. Qiao, L. Liu, C. Huang, K. Liu, X. Li, Z. Lu, T. Wang, General strategy to optimize gas evolution reaction via assembled striped-pattern superlattices, *J. Am. Chem. Soc.* 142 (2019) 1857–1863.
- [43] L. Guo, J. Chi, J. Zhu, T. Cui, J. Lai, L. Wang, Dual-doping NiMoO<sub>4</sub> with multi-channel structure enable urea-assisted energy-saving H<sub>2</sub> production at large current density in alkaline seawater, *Appl. Catal. B: Environ.* 320 (2023) 121977–121987.
- [44] Y.Y. Chen, Y. Zhang, X. Zhang, T. Tang, H. Luo, S. Niu, Z.H. Dai, L.J. Wan, J.S. Hu, Self-templated fabrication of MoNi<sub>4</sub>/MoO<sub>3-x</sub> nanorod arrays with dual active components for highly efficient hydrogen evolution, *Adv. Mater.* 29 (2017) 1703311–1703318.
- [45] Z. Zhang, X. Liu, D. Wang, H. Wan, Y. Zhang, G. Chen, N. Zhang, R. Ma, Ruthenium composited NiCo<sub>2</sub>O<sub>4</sub> spinel nanocones with oxygen vacancies as a high-efficient bifunctional catalyst for overall water splitting, *Chem. Eng. J.* 446 (2022) 137037–137047.
- [46] S. Chen, H. Huang, P. Jiang, K. Yang, J. Diao, S. Gong, S. Liu, M. Huang, H. Wang, Q.J.A.C. Chen, Mn-doped RuO<sub>2</sub> nanocrystals as highly active electrocatalysts for enhanced oxygen evolution in acidic media, *ACS Catal.* 10 (2019) 1152–1160.
- [47] Z. Yang, Y. Zhang, C. Feng, H. Wu, Y. Ding, H. Mei, P. doped NiCoZn LDH growth on nickel foam as an highly efficient bifunctional electrocatalyst for overall Urea-water electrolysis, *Int. J. Hydrog. Energy* 46 (2021) 25321–25331.
- [48] T. Cui, J. Chi, J. Zhu, X. Sun, J. Lai, Z. Li, L. Wang, Tuning the size and chemisorption of FeP<sub>4</sub> by trace Ru doping for hydrazine-assisted hydrogen evolution in seawater at large-current-density, *Appl. Catal. B: Environ.* 319 (2022).
- [49] L. Tan, J. Yu, C. Wang, H. Wang, X. Liu, H. Gao, L. Xin, D. Liu, W. Hou, T. Zhan, Partial sulfidation strategy to NiFe-LDH@ FeNi<sub>2</sub>S<sub>4</sub> heterostructure enable high-performance water/seawater oxidation, *Adv. Funct. Mater.* 32 (2022) 2200951–2200962.
- [50] L. Zhang, Y. Zhu, Z. Nie, Z. Li, Y. Ye, L. Li, J. Hong, Z. Bi, Y. Zhou, G.J. An Hu, Co/MoC nanoparticles embedded in carbon nanoboxes as robust trifunctional electrocatalysts for a Zn-air battery and water electrocatalysis, *ACS Nano* 15 (2021) 13399–13414.
- [51] J. Wan, Z. Zhao, H. Shang, B. Peng, W. Chen, J. Pei, L. Zheng, J. Dong, R. Cao, R. Sarangi, In situ phosphatizing of triphenylphosphine encapsulated within metal-organic frameworks to design atomic Co1–P1N3 interfacial structure for promoting catalytic performance, *J. Am. Chem. Soc.* 142 (2020) 8431–8439.
- [52] L. Wu, L. Yu, B. McElhenny, X. Xing, D. Luo, F. Zhang, J. Bao, S. Chen, Z. Ren, Rational design of core-shell-structured CoP@FeOOH for efficient seawater electrolysis, *Appl. Catal. B: Environ.* 294 (2021).